ADVANCED ENERGY MATERIALS
www.advenergymat.de

Multi-Parameters Self-Powered Monitoring via Triboelectric and Electromagnetic Mechanisms for Smart Transmission Lines

Xiaosong Zhang, Jianlong Wang, Shijie Zhai, Yang Yu, Xiaojun Cheng, Hengyu Li, Zhong Lin Wang,* and Tinghai Cheng**

The application of distributed sensors in smart transmission lines to replace traditional inspection methods is an inevitable trend. Currently, the challenge of energy supply for sensors serves as a bottleneck that hinders the intelligent development of transmission lines. This paper focuses on the application of self-powered inspection technology based on triboelectric and electromagnetic mechanisms in transmission lines. It proposes a self-powered temperature and vibration monitoring and warning system (STV-MWS) for multi-parameter monitoring of transmission line status. This work utilizes the quasi-zero stiffness structure and center misalignment design to improve the output performance of STV-MWS at low vibration amplitude, thereby extending its vibration amplitude response range. The STV-MWS is capable of harvesting and monitoring vibration of 50 µm and above vibration amplitude and 2–700 Hz vibration frequencies, which fully covers the breeze vibration range of transmission lines. Through the split package design, the flexible deployment of STV-MWS is achieved, further enhancing its engineering application value. This work can effectively ensure that the transmission line inspection can carry out accurate status monitoring and intelligent analysis in the environment characterized by steep terrain, challenging power extraction, and difficult fault judgment, thereby realizing the visualization and intelligence of the transmission line status.

1. Introduction

Being a pivotal infrastructure in the ongoing global energy construction, transmission lines play a crucial role in the energy supply network.[1,2] The transmission line possesses characteristics of wide distribution, considerable length, and towering height. Additionally, transmission lines are predominantly installed in mountainous, hilly, and other areas to prevent the wastage of land resources.[3] However, challenges such as high-risk mountain roads, low efficiency, and unforeseeable hazards significantly impede the daily inspection of the transmission lines.[4–6] Especially, conductor temperature and vibration state are particularly prominent problems affecting the normal operation of transmission lines, and constant vibration and temperature changes will directly affect the safety and efficiency of transmission lines. Therefore, it is necessary to monitor the temperature and vibration of the transmission line, which is the key to ensuring the operation status of the transmission line and the safety of the power grid operation. The development of digital technology can further propel the progress of intelligent inspection technology. It is noteworthy that the construction of an intelligent inspection network requires a large number of power sensors in the transmission lines.[7–9] However, traditional battery power cannot meet the needs of a large number of distributed layouts. Therefore, the issue of energy supply for power sensors is becoming increasingly prominent. Currently, environmental energy harvesting technology for smart transmission lines has been extensively studied,[10,11] with the most widely used methods being photovoltaic power generation and current transformers.[12–14] However, photovoltaic power generation technology is significantly affected by the environment and cannot obtain energy under adverse weather conditions such as rain, snow, or hail. Current transformer technology has the problems of core saturation and power dead zone and is exclusively applicable to alternating current (AC) transmission lines and cannot meet the growing demand for new ultra-high voltage direct current technology. Thus,

X. Zhang, J. Wang, S. Zhai, Y. Yu, X. Cheng, H. Li, Z. L. Wang, T. Cheng
Beijing Institute of Nanoenergy and Nanosystems
Chinese Academy of Sciences
Beijing 101400, P. R. China
E-mail: lihengyu@binn.cas.cn; zhong.wang@mse.gatech.edu; chengtinghai@binn.cas.cn

X. Zhang, J. Wang, S. Zhai, Y. Yu, X. Cheng, H. Li, T. Cheng
School of Nanoscience and Engineering
University of Chinese Academy of Sciences
Beijing 100049, P. R. China

X. Cheng, H. Li, Z. L. Wang, T. Cheng
Guangzhou Institute of Blue Energy
Guangzhou 510555, P. R. China

Z. L. Wang
Georgia Institute of Technology
Atlanta, GA 30332-0245, USA

The ORCID identification number(s) for the author(s) of this article can be found under https://doi.org/10.1002/aenm.202401710

DOI: 10.1002/aenm.202401710

there is an urgent need for a technology that can achieve continuous and stable energy harvesting even in adverse weather and under specific transmission conditions.

The research on vibration energy harvesting has a long history, and the main methods are electromagnetic generators (EMGs),[15–17] piezoelectric nanogenerators (PENGs),[18–21] triboelectric nanogenerators (TENGs),[22–25] and hybrid generators.[26,27] Compared with the vibrational EMGs, the output of vibrational PENGs and vibrational TENGs is relatively weak.[28,29] But the PENGs and TENGs have high voltage and signal sensitivity, their output signals are more applicable for vibration sensing in practical applications.[30–32] Among them, piezoelectric materials are fragile and prone to damage under prolonged exposure to high-frequency vibration. Therefore, it is more feasible to utilize EMGs for harvesting vibration energy as an energy supply and TENGs for achieving vibration condition monitoring.[33–35] Since the large-scale construction of overhead transmission lines in the early 20th century, it has been observed that these lines generate a significant number of vibrations with distinct characteristics due to factors such as wind and ice, including breeze vibration, sub-span oscillation, and galloping. Therefore, the application of vibration energy harvesting technology to achieve wind-induced vibration energy harvesting and self-powered sensing of transmission lines represents a novel solution to realize the self-powered monitoring of transmission lines.[36–39] It is worth noting that the breeze vibration of transmission lines persists for the longest duration and exhibits characteristics of a wide frequency range and small amplitude.[40] Consequently, the energy harvesting for breeze vibration of transmission lines requires to increase in the bandwidth and amplitude response range of the device.

Herein, a self-powered temperature and vibration monitoring and warning system (STV-MWS) is introduced based on the triboelectric vibration sensor (TVS) and vibration energy harvester (VEH) for the establishment of an intelligent inspection network for transmission lines. The quasi-zero stiffness and center misalignment structure aim to enhance the output performance of the TVS and VEH at low vibration amplitude, thereby extending the vibration amplitude response range of STV-MWS. Initially, theoretical modeling and mechanical analysis of the structural characteristics of the quasi-zero stiffness are conducted to optimize the structural parameters of the TVS. Subsequently, the output performance of TVS and VEH is tested to validate the vibration energy harvesting and self-powered sensing capabilities of STV-MWS. Finally, self-powered hardware circuits and monitoring and warning software for STV-MWS are developed. Additionally, temperature, humidity, vibration, and temperature rise monitoring and warning demonstrations are conducted to prove the feasibility of constructing an intelligent inspection network with STV-MWS for transmission lines.

2. Results and Discussion

2.1. Structural Framework Design and Working Mechanism of the STV-MWS

To meet the energy supply requirements of intelligent inspection for distributed sensors of transmission lines, a self-powered temperature and vibration monitoring and warning system (STV-MWS) based on triboelectric nanogenerators (TENGs) and electromagnetic generators (EMGs) is proposed. As shown in **Figure 1a**, the STV-MWS can be distributed at both ends of each pitch of transmission lines to achieve self-powered sensing of the temperature, humidity, and vibration status of transmission lines. Then, the sensing data at different locations is transmitted to the monitoring end by wireless transmission technology, creating an intelligent inspection network and enhancing the efficiency of inspection and fault elimination for transmission lines. The design of the STV-MWS is mainly directed against the wind-induced vibration of transmission lines, as shown in Figure 1b. The overhead transmission lines are usually installed at a height of more than 10 m above the ground. The leeward side of the aluminum conductor steel-reinforced produces alternating Karman vortex street due to wind action. Then the double-row line vortexes falling from the Karman vortex street causes the upper and lower alternating forces to act on the wire, causing the wire to produce vertical vibration. When the vortex frequency is similar to the wire resonance frequency, the wire produces a slight amplitude of high-frequency vibration, most of the frequencies are between 3–50 Hz, and the maximum vibration amplitude does not exceed 2 times the transmission line diameter (≈50 mm).[40] According to the above phenomena, the vibrational EMG and TENG are designed for energy harvesting and self-powered sensing of wind-induced vibration of transmission lines. The structural framework of the STV-MWS is shown in Figure 1c. The STV-MWS consists of five units: 1) vibration energy harvester (VEH) consisting of vibrational EMG with center misalignment structure; 2) triboelectric vibration sensor (TVS) consisting of vibrational TENG with quasi-zero stiffness structure; 3) commercial temperature and humidity sensor equipped with circuits; 4) self-powered hardware circuits consisting of power management unit and microcontroller unit; 5) data monitoring unit consisting of data receiver and visualization software. The VEH harvests the vibration energy from the transmission lines and stores it in the power management unit, which provides a stable power supply to the microcontroller unit. As the TVS is a passive sensor, it can transmit the sensing signal of vibration directly to the microcontroller unit, whereas the commercial temperature and humidity sensor must be powered by the power management unit to transmit the temperature and humidity signal to the microcontroller unit. The data processed by the sensing signal is transmitted to the data monitoring unit via the microcontroller unit. Then, the data visualization display and warning are carried out in the data monitoring unit, which can realize the construction of the intelligent inspection network of transmission lines.

Based on the triboelectric and electrostatic induction coupling effect, TENG converts mechanical energy into electrical energy using displacement current as the driving force. In contrast to TENG, the electromechanical energy conversion process of EMG is mainly driven by conduction current. To illustrate the electromechanical energy conversion process of TVS and VEH, the current generation mechanism of vibrational TENG and vibrational EMG under periodic sinusoidal vibration is analyzed. As shown in **Figure 2a(i)**, the vibrational TENG adopts vertical contact-separation mode. The upper and lower acrylic plates are pasted with a copper film and a nylon film in turn, and the copper films of the upper and lower plates are connected to an external load. The vibrator consists of an acrylic box with a mass in the

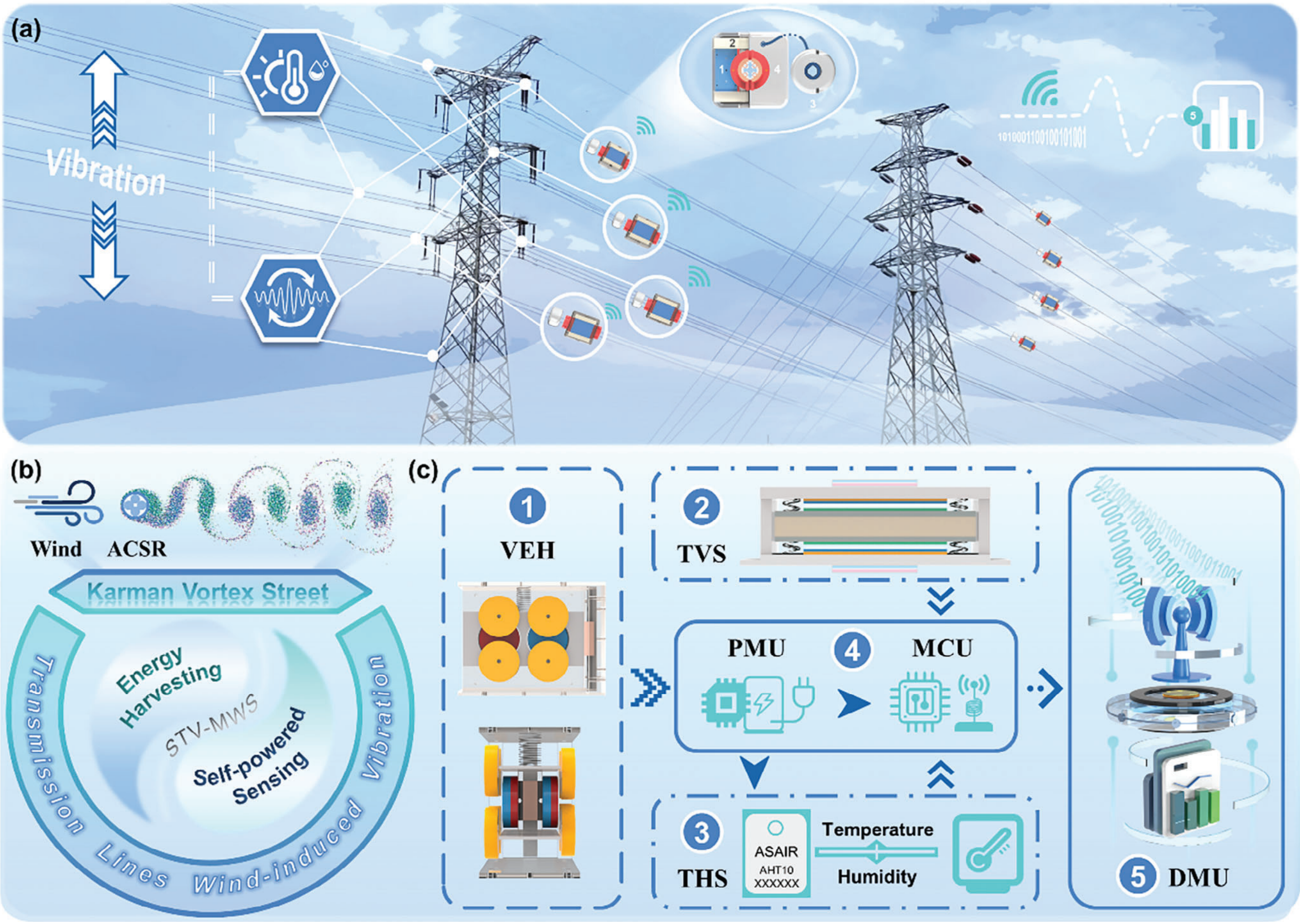

Figure 1. Design of the self-powered temperature and vibration monitoring and warning system (STV-MWS). a) Schematic diagram of the STV-MWS in the transmission lines. b) Wind-induced vibration process of transmission lines. c) Structural framework of the STV-MWS.

center and a layer of fluorinated ethylene propylene (FEP) film on both sides. Due to the difference in triboelectric polarity, contact between the nylon and FEP films produces opposite charges on their surfaces. It is worth noting that polymer materials have good insulating properties, and their surface charge can be maintained for a long time. It is therefore assumed that the surface of the nylon and FEP films is evenly covered with the same amount of opposite charges. In the initial state, the vibrator is placed in the central position of the upper and lower plates. As the vibrational TENG vibrates upwards, the distance between the vibrator and the lower plate gradually decreases due to inertia. In this case, a potential difference occurs between the two copper films due to electrostatic induction. To balance the potential difference, the positive charge is transferred from the copper film of the upper plate to that of the lower plate through an external load, creating a current in the external load. The electrostatic balance is restored when the vibrator comes into contact with the lower plate. The vibrator then gradually moves away from the lower plate. As the distance between the vibrator and the upper plate decreases, the charge from the copper film of the lower plate flows back into that of the upper plate. At this time, the external load generates the opposite current. As a result, vibrational TENG generates an alternating current (AC) signal during continuous relative vibration.

For the vibrational EMG, the coils are mounted in acrylic plates on both sides, and the magnets are suspended in the center position by a spring. When the magnets move up and down due to external vibration, the magnetic field in the coils on either side changes. The change in the magnetic flux of the coil produces an induced electromotive force based on Faraday's law of electromagnetic induction. At this point, the current is generated in the coil, converting the mechanical energy into electrical energy.

To illustrate the relationship between the output signal of the vibrational TENG and the motion of the vibrator, the vibrational TENG is simulated by the COMSOL software. As shown in Figure 2b, when the vibrator comes into contact with the upper or lower plate, the output voltage of vibrational TENG reaches a saturation value. And when the vibrator reaches the middle of the two plates, the output voltage is 0 V. The voltage signal output by the vibrational TENG corresponds to the change of vibration displacement during one vibration period, which is consistent with the above analysis of the working mechanism. It is further indicated that the regular voltage signal generated by the TVS can reflect the state of environmental vibration.

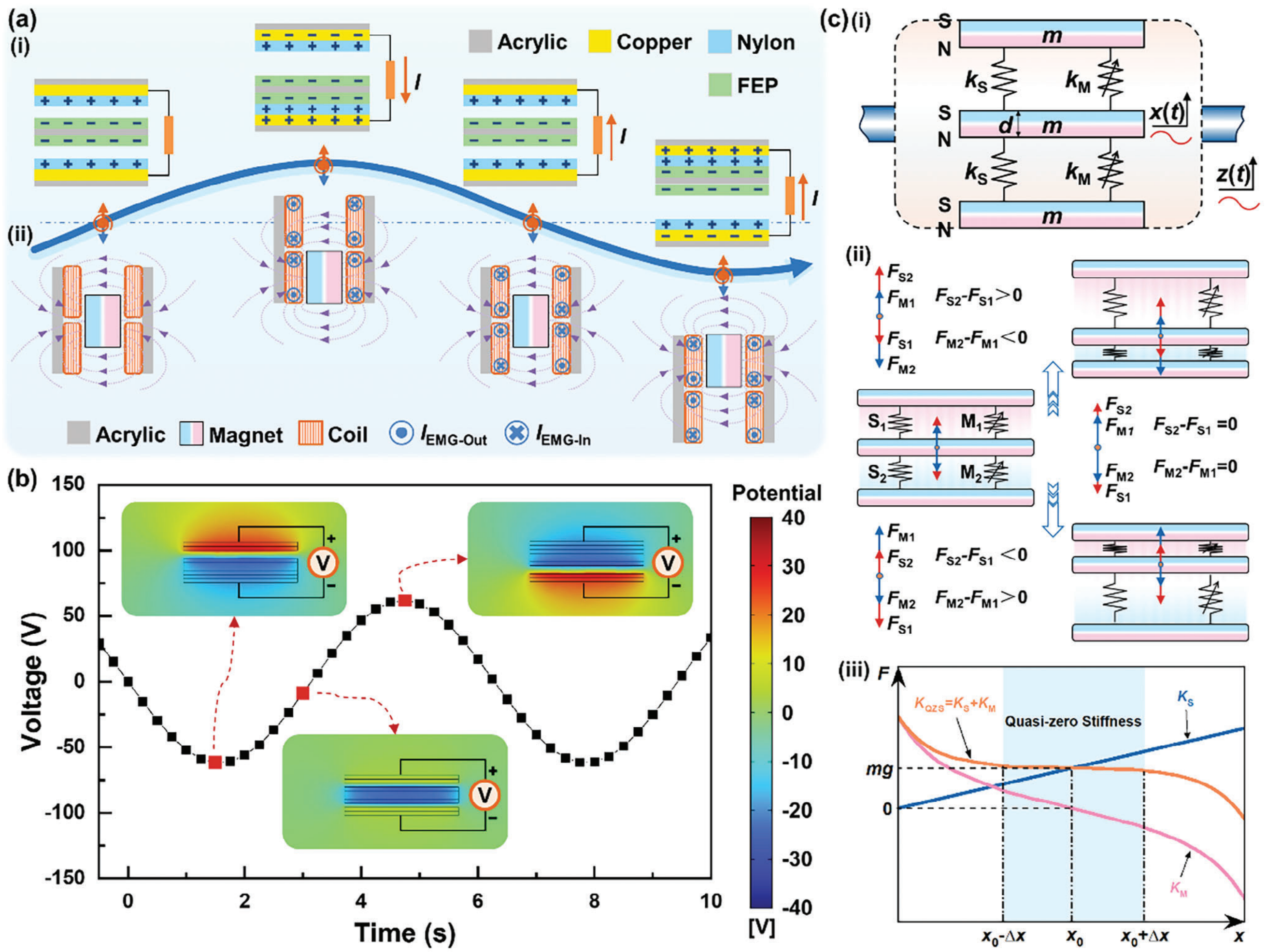

Figure 2. Electromechanical energy conversion process and structural characteristics analysis of STV-MWS. a) Electromechanical energy conversion process of i) triboelectric vibration sensor (TVS) and ii) vibration energy harvester (VEH). b) COMSOL simulation results of TVS at different positions. c) Quasi-zero stiffness i) modeling and (ii and iii) force analysis of TVS.

The vibrational TENG in Figure 2a is a traditional sandwich structure. To improve the response performance of TVS in the low vibration amplitude range, an axial negative stiffness structure is innovatively introduced in the vibrational TENG to achieve quasi-zero stiffness vibration. As shown in Figure 2c(i), two springs with a stiffness of k are connected to the upper and lower plates, and the spring force k_S provides positive stiffness to the vibrator. Three magnets with mutual attraction in the TVS are arranged in the vibration direction of the vibrator. The center magnet is designed inside the vibrator, to vibrate freely in the vertical direction with the vibrator. The other two magnets are fixed on the upper and lower plates, respectively. Therefore, the magnetic force k_M generated by the magnet provides the vibrator with a negative stiffness opposite to the spring force k_S.

To further illustrate the negative stiffness structure of TVS, the force analysis of its motion process is carried out. As shown in Figure 2c(ii), it is assumed that the vibrator is only affected by the spring force F_S and magnetic force F_M, and its static equilibrium position is located at the vertical center of the TVS. At this point, the upper and lower springs are in compression, and the compression displacement is equal. And the magnets on both ends are at equal distances. Therefore, the total spring force and the total magnetic force acting on the vibrator are zero. When the vibrator moves downwards under the external vibration, the distance between the vibrator and the lower plate decreases, and the distance between the vibrator and the upper plate increases. At this time, the spring force F_{S1} and the magnetic force F_{M1} increase, while the magnetic force F_{M2} and the spring force F_{S2} decrease. Their relationship is as follows:

$$F_{S2} - F_{S1} > 0 \tag{1}$$

$$F_{M2} - F_{M1} < 0 \tag{2}$$

In the same way, when the vibrator moves upward, the distance between the vibrator and the lower plate increases, and the distance between the upper plate decreases. At this time, the spring force F_{S1} and the magnetic force F_{M1} decrease, while the magnetic force F_{M2} and the spring force F_{S2} increase. Their relationship is as follows:

$$F_{S2} - F_{S1} < 0 \tag{3}$$

$$F_{M2} - F_{M1} > 0 \tag{4}$$

The effect of the springs on the vibrator is defined as positive stiffness. Since the magnetic force is in the opposite direction to the spring force, the effect of the magnets on the vibrator is defined as negative stiffness. The coupling effect of magnetic force and spring force weakens the influence of the positive stiffness of the springs on the vibrator during vibration, and the total recovery force of the vibrator decreases. It can be understood that the motion resistance of the vibration when it vibrates under the influence of external vibration is weakened so that the vibrator has better response sensitivity under weak vibration excitation.

The magnetic force F_M of two magnets that are attracted to each other at a distance d from each other is expressed as:

$$F_M = \frac{C_M}{d^2} \tag{5}$$

where C_M is the magnetic constant, which depends on the strength of the magnets and the medium in which they are located.

When the vibrator is in the center equilibrium position, the springs are compressed. Assuming that the compression is h, then the force F_S of the springs on the vibrator can be regarded as:

$$F_S = k_S h \tag{6}$$

where k_S is the elasticity coefficient, which depends on the material, shape, and size of the springs.

The force (the pink line in Figure 2c(iii)) of the magnets acting on the vibrator magnet as the vibrator of the TVS moves x displacement from the central position is:

$$F_{M1+M2} = -C_M \frac{4dx}{\left(d^2 - x^2\right)^2} \tag{7}$$

At this point, the force (the blue line in Figure 2c(iii)) of the springs acting on the vibrator is:

$$F_{S1+S2} = 2k_S x \tag{8}$$

So, the relationship between the coupling force F_{QZS} (the yellow line in Figure 2c(iii)) and the displacement of the mass is:

$$F_{QZS} = 2k_S x - C_M \frac{4dx}{\left(d^2 - x^2\right)^2} \tag{9}$$

According to Equations (7)–(9), the relationship between force and displacement in Figure 2c(iii) can be obtained. Assuming that the intersection of the spring force and gravity is the equilibrium position x_0, the coupling force F_{QZS} near the equilibrium position ($x_0 \pm \Delta x$) is approximately equal to the gravity. At this range, it can be considered that the vibrator is in the quasi-zero stiffness state due to the negative stiffness, which improves the response performance of the vibrational TENGs at low amplitudes.

2.2. Basic Performances of the STV-MWS

According to the above theoretical model, the influence of magnetic force generated by magnets of different thicknesses on the quasi-zero stiffness state is explored to obtain a wide quasi-zero stiffness range. As shown in **Figures** 3a and S1 (Supporting Information), magnets with a thickness of 1 to 3 mm are selected for the simulation. The relationship curve between elastic recovery force and displacement of the constructed quasi-zero stiffness system is nonlinear (Figure S2, Supporting Information). The smaller the thickness of the magnet it has, the less magnetic force it can generate, and the closer the coupling force is to 0 N after interacting with the spring force (Figure 3a(i)). In this case, the stiffness of the system near the static equilibrium position tends to be 0 N mm^{-1} and the quasi-zero stiffness range is larger (Figure 3a(ii)). Therefore, the magnets with 1 mm thickness are selected to develop the TVS prototype.

To verify the output effect of the prototypes, a vibration excitation and experimental system is built (Figure S3 and Note S1, Supporting Information). The output performance of vibrational TENGs with or without quasi-zero stiffness structure is compared. As shown in Figure 3b and Movie S1 (Supporting Information), the vibrational TENG with quasi-zero stiffness structure exhibits higher output performance at different amplitudes than the conventional vibrational TENG. From the performance increase results shown in Figure S4 (Supporting Information), the maximum increase rate for the open-circuit voltage output by the TVS with quasi-zero stiffness structure can reach 214%.

Subsequently, to study the basic sensing performance of the TVS, the frequency response characteristics of TVS under three vibration amplitudes are first measured. As shown in Figure 3c(i) and Figure S5 (Supporting Information), the TVS can output good open-circuit voltage signals from 2 to 60 Hz at 0.05, 0.5, and 2 mm vibration amplitudes, respectively, and the maximum open-circuit voltage is 59.2 V. The fast Fourier transform is performed on the open-circuit voltage signals to obtain the frequency of the signal. According to the simulation results in Figure 2b, the frequency of the open-circuit voltage output by the TVS should be the same as the vibration frequency. As shown in Figure 3c(ii), the output frequency of the open-circuit voltage has good linearity with the vibration frequency at the different vibration amplitudes, which is basically the same as $y = x$. Therefore, the frequency of the open-circuit voltage output by the TVS can be used as the vibration monitoring frequency of STV-MWS. Subsequently, the error rate of the TVS at different frequencies is analyzed shown in Figure 3c(iii). The error values of TVS are kept within the range of ±0.05 Hz under different vibration frequencies, and the average error rate decreases with the increase of vibration frequency. The maximum error rate is less than 1% in the common vibration frequency range of 3–50 Hz for transmission lines. In addition, the TVS also exhibits good linear frequency control in the 60–700 Hz range, extending the range of applications for the TVS (Figure 3d; Figure S6a, Supporting Information). The short-circuit currents and open-circuit voltage curves output in the corresponding range are shown in Figure S6b,c (Supporting

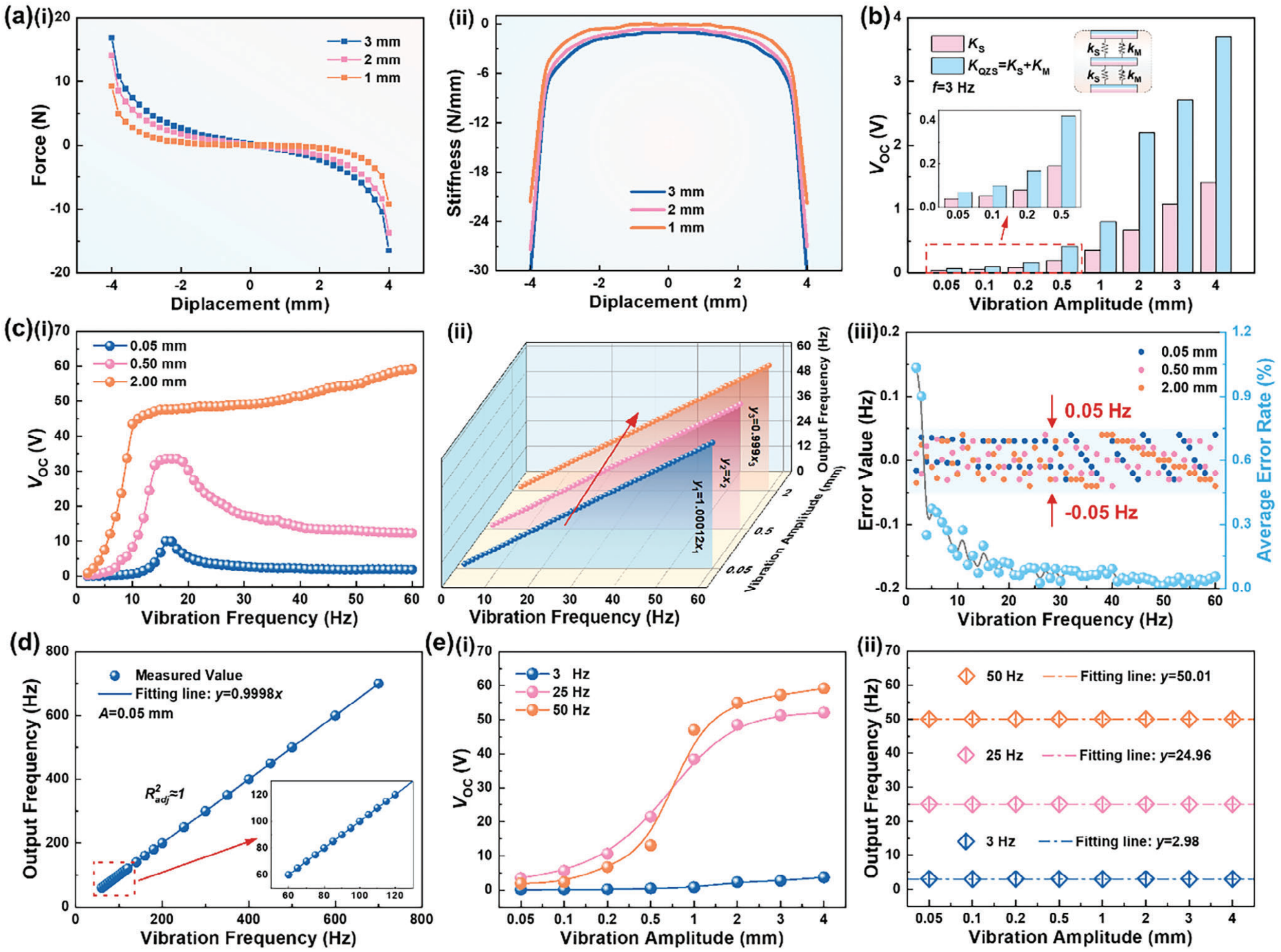

Figure 3. Sensing performance of TVS. a) Simulation results of i) static properties and ii) coupling stiffness of the quasi-zero stiffness model with different thicknesses of magnets. b) Comparison of open-circuit voltages of TVS with and without quasi-zero stiffness structure at different vibration amplitudes. c) i) Open-circuit voltage, ii) frequency characteristics, and iii) error analysis of TVS at different vibration frequencies. d) Frequency characteristics at vibration frequencies of 60–700 Hz. e) i) Open-circuit voltage, ii) frequency characteristics at different vibration amplitudes.

Information). Finally, the output performance of TVS under different vibration amplitudes is studied. As shown in Figure 3e(i) and Figure S7 (Supporting Information), the open-circuit voltage output by the TVS increases as the vibration amplitude increases. However, the signal frequencies of the TVS also maintained good repeatability at different vibration amplitudes (Figure 3e(ii)). The accuracy and stability of the vibration frequency monitoring of TVS are demonstrated.

Extending the amplitude response range of the VEH is also an important indicator. Therefore, we propose a center misalignment structure, as shown in **Figure** 4a. When the central position of the vibrational magnet is aligned with the circumferential boundary of the coil, the output signal of the vibrational EMG at low-amplitude vibration is greatly improved compared to the traditional center alignment design. This is because the magnetic induction lines of a circular magnet are less dense the further away from the center of the magnet. Therefore, the amount of change in the magnetic induction lines within the coil of the center misalignment structure is greater than that of the center alignment structure under the low-amplitude vibration. As shown in Figure 4b, the output performance of the two structures is compared to verify the feasibility of the center misalignment structure. The output performance of the VEH with the center misalignment structure is greater than that of the VEH with the center misalignment structure, and the maximum increase rate of open-circuit voltage and short-circuit current can reach 883% and 900%, respectively (Figure S8, Supporting Information). The above results prove that the center misalignment structure can achieve good performance output at low amplitude, thereby broadening the amplitude response range of VEH.

To further enhance the output performance of VEH, we have optimized the coil arrangement. Depending on the position of the coils of the center misalignment structure, multiple symmetrically arranged coils are connected in series. The open-circuit voltage and short-circuit current of VEH with various numbers of coils connected in series at different vibration amplitudes are illustrated in Figure 4c and Figure S9 (Supporting Information), respectively. The open-circuit voltage increases exponentially with the number of series, while the short-circuit current essentially remains. In addition, the open-circuit voltage and

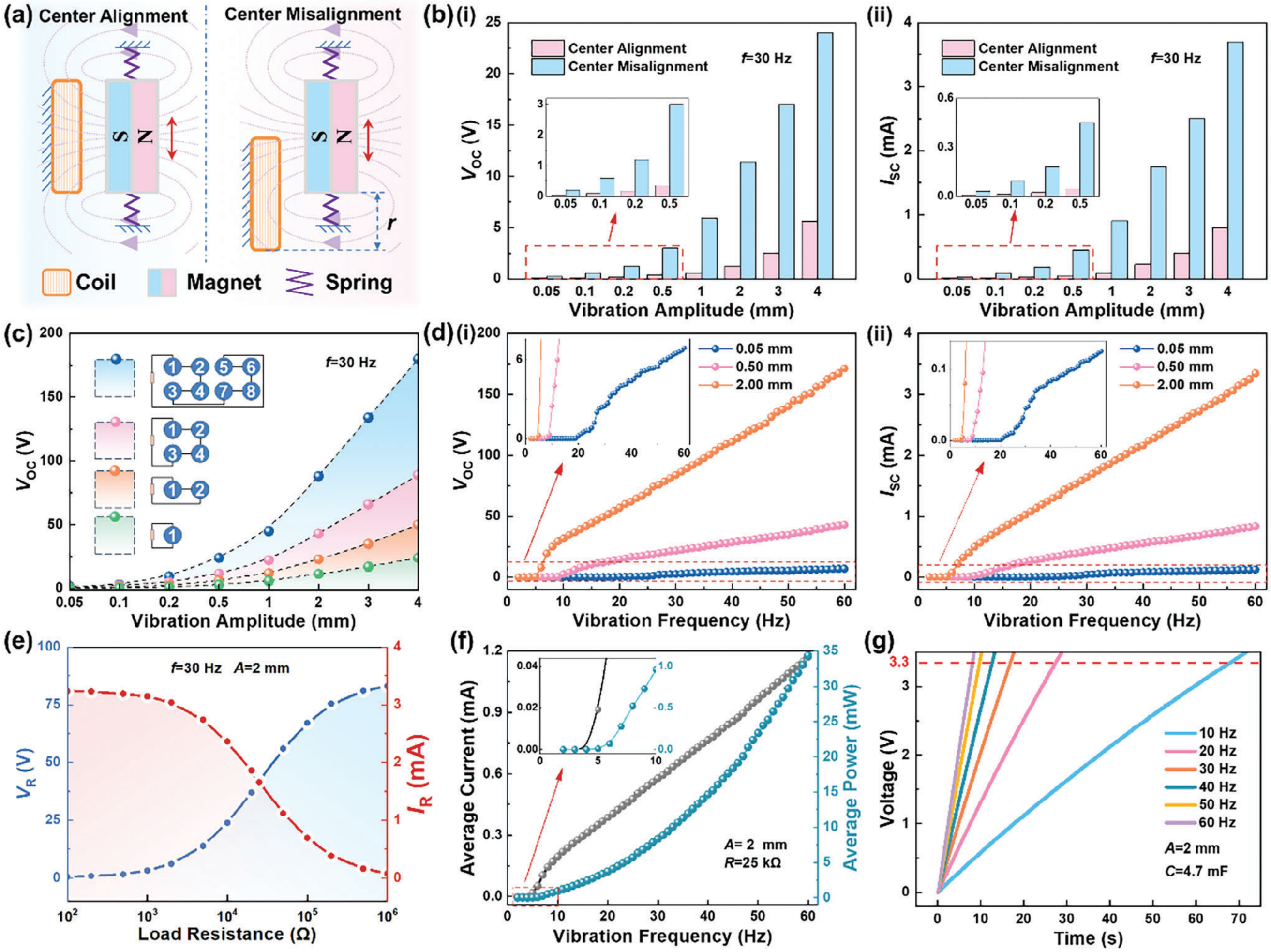

Figure 4. Energy harvesting performance of the VEH. a) Schematic diagram of the layout of the VEH. b) Comparison of i) open-circuit voltage and ii) short-circuit current output by VEH with different layouts under different vibration amplitudes. c) Open-circuit voltage of the series coil. d) i) Open-circuit voltage and ii) short-circuit current output by VEH under different vibration frequencies. e) Voltage and current of VEH at different load resistances. f) Average current and average power output by VEH at different vibration frequencies. g) Charge capacity curves of VEH at different vibration frequencies.

short-circuit current increase with the vibration amplitude. Therefore, we select 8 series coils to manufacture the VEH prototype. Subsequently, the frequency response characteristics of VEH are tested. As shown in Figure 4d, the open-circuit voltage and short-circuit current of the VEH show an upward trend as the frequency increases, and the trend is basically the same. At the vibration amplitude of 2 mm and the vibration frequency of 60 Hz, the maximum open-circuit voltage and short-circuit current can reach 171.2 V and 3.345 mA, respectively. The output curves at some frequencies are shown in Figures S10 and S11 (Supporting Information). To illustrate the actual energy harvesting performance of VEH, its output power and charge capacity characteristics are tested. As shown in Figure 4e, as the external load increases, the load voltage tends to decrease while the load current tends to increase. Based on the above results, the peak power curve of the VEH can be calculated. As shown in Figure S12 (Supporting Information), the VEH achieves a peak power of 70.56 mW with an optimal load of 25 kΩ. The optimal load basically corresponds to the resistance of the series of coils. Therefore, the output performance of the VEH is measured at different vibration frequencies and 25 kΩ load. As shown in Figure 4f, the average power of a VEH increases with the vibration frequency, and the maximum average power of a VEH can reach 34.375 mW. At this point, the power density of the VEH can reach 294 W m^{-3}. Finally, the capacitors are charged at different vibration frequencies using VEH. As shown in Figure 4g and Figure S13 (Supporting Information), the VEH can charge a 4.7 mF capacitor to 3.3 V in 70 s at a vibration frequency of 10 Hz and a vibration amplitude of 2 mm. At a vibration frequency of 60 Hz, the VEH can accomplish this in less than 8 s. The above experiments show that VEH has good energy harvesting performance in the vibration range of transmission lines.

The circuit design is key for the self-powered sensing of the STV-MWS. As shown in **Figures** 5a and S14 (Supporting Information), the self-powered hardware circuit architecture is designed based on the performance characteristics of VEH and TVS. It is worth mentioning that we design a circuit for low power consumption. The relays control the on/off of the power supply

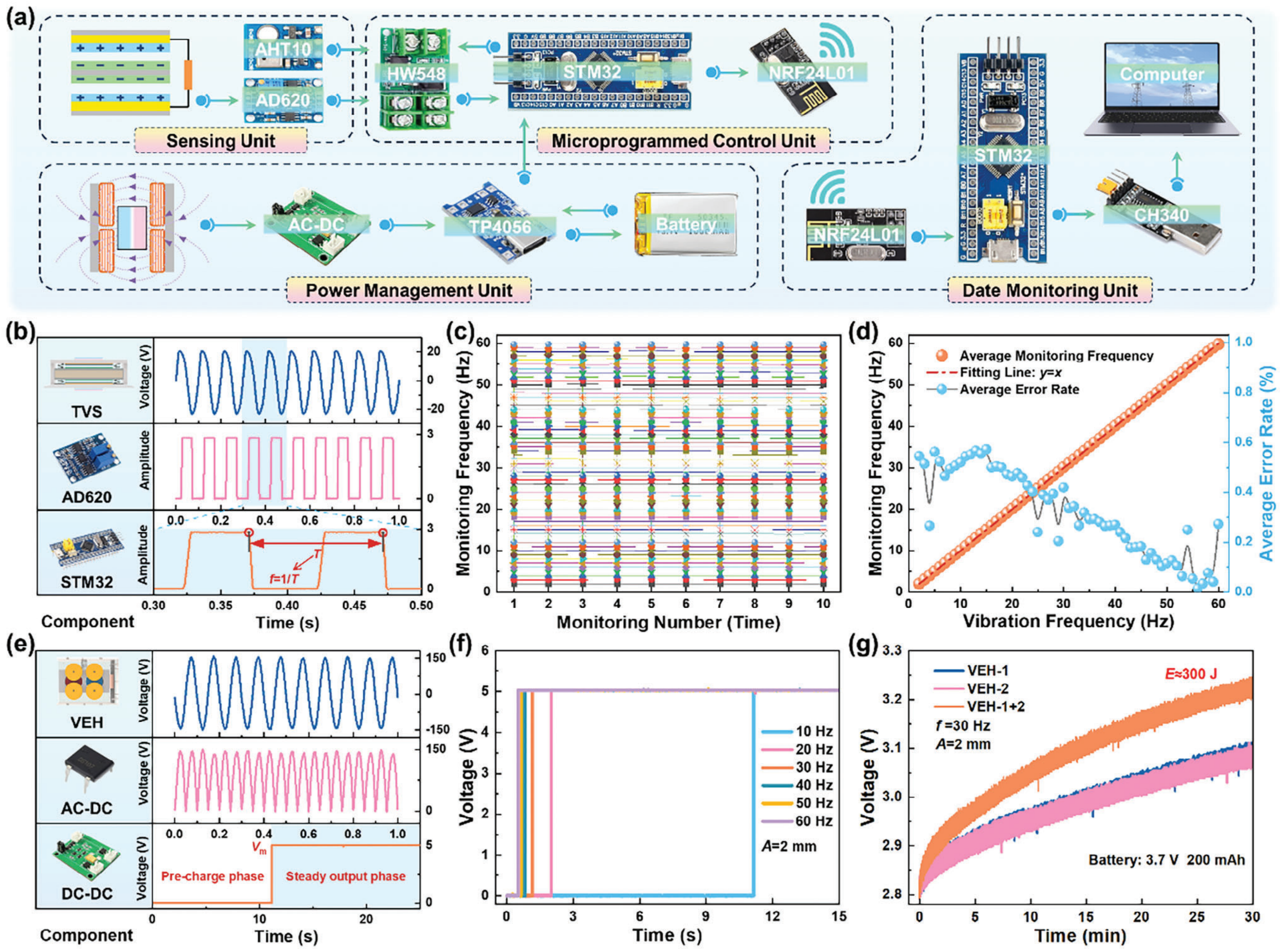

Figure 5. Self-powered hardware circuits design of STV-MWS. a) Schematic diagram of self-powered hardware circuit architecture of STV-MWS. b) Vibration signal processing process of TVS. c) Repeated performance of STV-MWS monitoring frequencies under different vibration frequencies. d) Linearity and error rate of STV-MWS monitoring frequencies at different vibration frequencies. e) Vibration energy harvesting process of VEH. f) Pre-charge performance of STV-MWS at different vibration frequencies. g) Charging performance of STV-MWS equipped with different amounts of VEH for charging lithium-ion battery.

circuits of sensors and wireless transmitters, thus reducing the power consumption of the circuits (Note S2, Supporting Information). The output performance of the TVS and VEH with hardware circuits is then tested separately. As shown in Figure 5b, the AC signal output by the TVS is first amplified and square-wave processed by the signal amplifier. Then, the time difference between the two adjacent falling edge points is calculated by the microcontroller unit, and the monitored frequency is obtained by deriving the time difference. Finally, it is transmitted to the computer for display via a wireless module. The frequencies received by the computer are analyzed, and the specific results are shown in Figure 5c,d. The 10 randomly received frequency signals have good repeatability and linearity under different vibration frequencies, and the average error rates are less than 0.6%. As shown in Figure 5e, the VEH acts as an energy harvesting source, the AC signal output by the VEH is first converted to a direct current (DC) signal via a rectifier bridge. The DC signal is then converted to a stable DC signal with a voltage of V_m (5 V) by the DC-DC converter and supplied to the battery for energy storage. The DC-DC conversion process is mainly divided into two phases: the pre-charging phase and the stable output phase. The pre-charging phase is mainly to meet the initial starting energy of the DC-DC converter, and the time it takes determines the initial charging speed of the VEH. Therefore, the DC-DC conversion process at different vibration frequencies is measured. As shown in Figure 5f, the pre-charge time of VEH decreases as the vibration frequency increases. The pre-charge time of the VEH is only ≈0.5 s at a vibration frequency of 60 Hz. Even when the vibration frequency is 10 Hz, the VEH can also reach a stable output state within 12 s. Finally, the charging performance of VEH for the lithium-ion battery is verified. To improve the energy harvesting efficiency and take into account the mass symmetry of the device, two VEHs are symmetrically installed in the prototype of the STV-MWS. As shown in Figure 5g, the charging performance of the two VEHs alone is basically the same, and the two VEHs together can charge the 200 mAh lithium-ion battery from 2.8 V to more than 3.2 V in 30 min, and the actual charging energy can reach 300 J (Movie S2, Supporting Information).

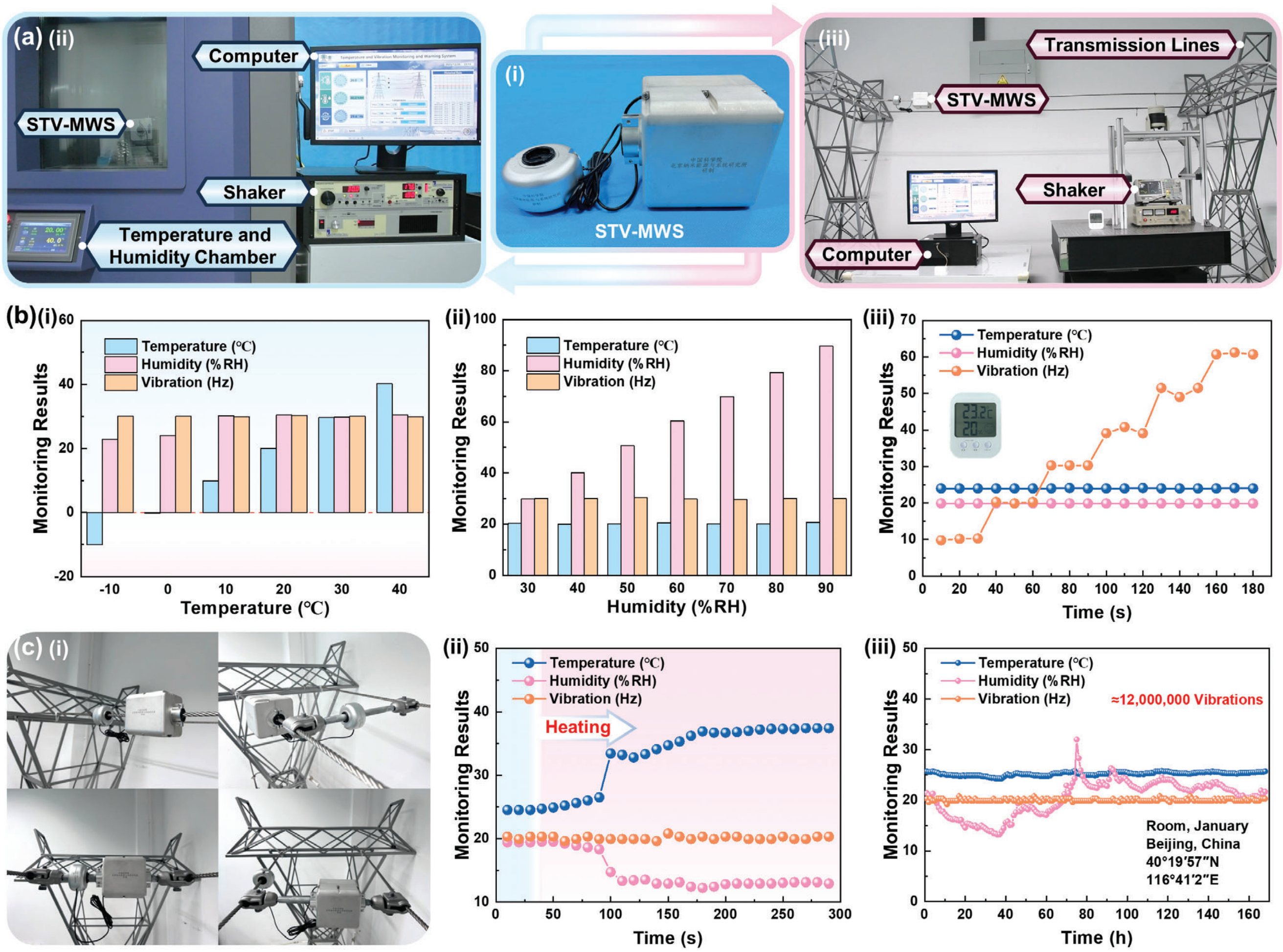

Figure 6. Application of STV-MWS in smart transmission lines. a) Photographs of i) prototype, ii) environment simulation system, and iii) transmission line vibration simulation system of STV-MWS. b) Sensing performance for i) temperature, ii) humidity, and iii) vibration of STV-MWS in the environmental simulation system. c) i) Photographs of the installation of STV-MWS on transmission lines, ii) temperature rise monitoring for transmission lines, and iii) long-term monitoring in the transmission line vibration simulation system.

These results demonstrate the feasibility of STV-MWS to realize vibration energy harvesting and self-powered sensing in intelligent inspection networks of transmission lines.

3. Demonstration of STV-MWS

To improve the anti-environmental interference of the device and to meet the condition monitoring requirements of different areas of transmission lines, a split package structure design is proposed. The prototype and internal details are shown in **Figure** 6a(i) and Figure S15 (Supporting Information). It is mainly divided into two parts: vibration energy harvesting and sensing module and temperature and humidity sensing module. First, considering the harsh external environment of the transmission line, it is necessary to improve the reliability and safety of the prototype in the natural environment through packaging design. Therefore, the VEH, TVS, and hardware circuits are integrated into vibration energy harvesting and sensing modules and packaged to meet the engineering application requirements in the harsh environment of transmission lines. Meanwhile, the temperature and humidity sensing module is designed as an external split structure to allow a flexible arrangement of vibration energy harvesting and sensing module and temperature and humidity sensing module, which can realize temperature and humidity monitoring in different parts of the transmission line. In addition, temperature and vibration monitoring and warning software is developed based on LabVIEW software to realize the visual monitoring and warning of the transmission line state (Figure S16 and Note S3, Supporting Information).

To verify the stability of multi-parameter self-powered monitoring of STV-MWS, an environmental simulation system with controllable temperature, humidity, and vibration is built (Figure 6a(ii); Note S4, Supporting Information). First, the temperature and humidity monitoring performance of the STV-MWS is investigated. Figure S17 (Supporting Information) shows the installation layout of the STV-MWS in the environmental simulation system. The monitoring process is shown in Movies S3 and S4 (Supporting Information), and the average monitoring results are shown in Figure 6b(i),(ii). This is followed by a demonstration of the monitoring performance of the

STV-MWS at various vibration frequencies at room temperature. As shown in Movie S5 (Supporting Information) and Figure 6b(iii), the monitoring process of the STV-MWS is observed in 10 Hz increments from 10 to 60 Hz. At different external application conditions, the temperature, humidity, and vibration monitored by the STV-MWS are basically consistent with the external state. The above demonstrations prove that the STV-MWS can monitor the parameters of temperature, humidity, and vibration of transmission lines in a stable and accurate manner.

To more realistically simulate the actual application environment, a transmission line vibration simulation system is built (Figure 6a(iii)). Transmission lines and multi-split spacers are important parts of the power system. The spacers are installed between multi-split transmission lines and synchronized vibrate with the conductors to prevent collision or entanglement when the transmission lines vibrate. Therefore, monitoring their condition can not only extend the service life of the spacers but also ensure the stable operation of the power system. Figure 6c(i) simulates the installation of STV-MWS on transmission lines and spacers, which demonstrates that the split package structure of STV-MWS can be flexibly applied to the installation and monitoring of transmission lines and spacers to meet engineering needs.

As the transmission lines run outdoors all year round, it is affected by the corrosion, aging, vibration, and other factors of the external environment, resulting in the wires, joints, wire clamps, and other parts of the transmission line and gasket being easy to heat. At present, the power industry mainly uses traditional methods such as periodic inspection and temperature measurement to determine the temperature of the hot spots of the wire. However, due to the inability to reflect the conductor temperature in time, the conductor temperature rise still often causes a large number of electrical accidents. The construction of the intelligent inspection network subverts the traditional manual inspection method, and the STV-MWS can be used to monitor the temperature, humidity, and vibration of the transmission lines and spacers in real time. The temperature rise monitoring application is carried out in the transmission line vibration simulation system. The STV-MWS is installed as shown in Figure 6c(i) with a vibration frequency of 20 Hz. As shown in Figure 6c(ii), the transmission line in the vicinity of the temperature and humidity sensing module is heated after a period of normal operation of the STV-MWS. The temperature rise can then be monitored on the software, and when the temperature exceeds a set threshold, the software will issue a high-temperature alarm. The demonstration process is shown in Movie S6 (Supporting Information). Finally, to verify the sustainability of the STV-MWS, the status of the transmission lines is continuously monitored for one week. The STV-MWS is treated with low power consumption, and the monitoring period is set to 1 h. As shown in Figure 6c(iii), the STV-MWS can accurately monitor the status of the transmission line during a week of continuous testing, which vibrates more than 12 million times. Finally, we conducted a rain experiment on the prototype for half an hour (Figure S18 and Note S5, Supporting Information) and electromagnetic shielding experiments (Figure S19 and Note S6, Supporting Information) to verify that it has good waterproof and anti-electromagnetic interference performance.

In addition, as shown in Table S1 and Note S7 (Supporting Information), the performance of this work is compared with the performance of some existing self-powered sensing systems for transmission lines, which shows that STV-MWS has good output performance and environmental adaptability. The successful demonstration of the above applications proves the feasibility of using STV-MWS to realize all-weather, self-powered, and wireless intelligent inspection of transmission lines.

4. Conclusion

In summary, we developed a self-powered monitoring and warning system for temperature, humidity, and vibration monitoring of transmission lines, which was able to obtain vibration energy as low as 50 μm through the quasi-zero stiffness and central misalignment structural characteristics. This work combines environmental energy harvesting, self-powered sensing, and wireless communication. Through the theoretical modeling and parameter optimization of quasi-zero stiffness, the output performance of the TVS could be improved by up to 214% under low amplitude conditions. Additionally, the sensing performance of the TVS was systematically tested. The TVS was capable of realizing vibration monitoring in the range of 2–700 Hz, and its error rate was less than 1%, effectively covering the breeze vibration monitoring range of transmission lines. Subsequently, the VEH with a center misalignment structure design was verified. The results have indicated that, compared with the traditional center alignment structure, the output voltage and current of the VEH with center misalignment design could be increased by up to 883% and 900%, respectively. Its maximum average power and power density reached 34.375 mW and 294 W m^{-3}, respectively. Furthermore, the feasibility of energy harvesting and self-powered sensing of the STV-MWS was demonstrated through the design of self-powered hardware circuits and monitoring and warning software. Considering the harsh outdoor environment of transmission lines, the STV-MWS was designed with a split package to enhance its practical engineering application. Ultimately, the application capability of STV-MWS was successfully verified, further emphasizing its engineering application value in the construction of an intelligent inspection network for transmission lines. This work has proposed a comprehensive solution to integrate vibration energy harvesting and self-powered sensing technology into the intelligent inspection of transmission lines, thereby promoting the integration of self-powered sensing technology and smart transmission lines.

5. Experimental Section

Manufacture of the STV-MWS: The STV-MWS consists mainly of mechanical devices, circuits, and software. The mechanical devices include VEH, TVS, and encapsulated housing. The encapsulated housing consists of two symmetrical parts that were screwed together for easy installation. All were made of aluminum materials, which have a good shielding effect against high-frequency electromagnetic waves and are conducive to heat dissipation of internal electrical components. The encapsulated housing also can improve the dustproof and waterproof performance of the prototype. In addition, as shown in Figure S20a (Supporting Information), TVS and VEH inside the prototype were encapsulated to enhance the environmental adaptability of the prototype. And the circuit was covered with silicone sealant to further enhance the waterproof performance of the circuit.

Manufacture of the VEH: The VEH mainly consists of an empty cuboid support frame, a vibrator, a spring, 4 magnets, and 8 coils. The cuboid support frame and vibrator were made of acrylic material. The magnet was an N52 round magnet with a diameter of 20 mm and a thickness of 5 mm. There were 2 magnets mounted on the left and right sides of the vibrator. The spring connects the upper plate of the cuboid support frame to the vibrator so that the vibrator with the magnet was suspended. The coil was made of copper, with a diameter of 20 mm and a thickness of 4 mm. The left and right sides of the cuboid support frame were fitted symmetrically with 4 coils each. The VEH resistance and inductance were tested using an LCR digital bridge (VICTOR 4092D), and the results are shown in Figure S20b (Supporting Information). The resistance is 28.5 kΩ, which is basically the same as the optimal impedance of 25 kΩ obtained in Figure 4(e), and the inductance is 5.36 H.

Manufacture of the TVS: The TVS consists mainly of an empty cuboid support frame, a vibrator, 8 springs, 3 magnets, some masses, and a TENG unit. The cuboid support frame and vibrator were made of acrylic material. The square magnets were made of N35, magnets with a length of 20 mm, a width of 10 mm, and a thickness of 1 mm. The three magnets were installed successively on the upper plate of the cuboid support frame, the center of the vibrator, and the lower plate of the cuboid support frame along the direction of vibration. Some masses were attached to the center of the vibrator to increase the motion inertia of the vibrator so that the total mass of the vibrator is 33 g. The diameter of the spring wire is 0.2 mm, the outer diameter is 4 mm, and the length is 5 mm. Eight springs were symmetrically mounted on the upper and lower sides of the vibrator, and the cuboid support frame was compressed against each other to suspend the vibrator in the middle position. In actual assembly, because the center vibrator has a relatively large mass, it cannot be completely ignored. To take into account the static displacement of the vibrator due to gravity and ensure the symmetry of the magnetic force, a sponge of ≈1 mm was inserted between the lower springs and the base plate, as shown in Figure S21 (Supporting Information). The lower springs were further compressed, providing excess spring force to resist the downward gravitational force. The TENG unit uses a 0.3 mm thick sponge and 80 μm thick copper film. The FEP thickness on the upper and lower sides of the vibrator is 30 μm, and the nylon thickness in the electrodes of the upper and lower plates is 25 μm.

Supporting Information

Supporting Information is available from the Wiley Online Library or from the author.

Acknowledgements

X.Z., J.W., and S.Z. contributed equally to this work. This research was supported by the Beijing Natural Science Foundation (Nos. 3222023 and 3244038).

Conflict of Interest

The authors declare no conflict of interest.

Data Availability Statement

The data that support the findings of this study are available from the corresponding author upon reasonable request.

Keywords

intelligent inspection, multi-parameter monitoring, self-powered sensing, smart transmission lines, vibrational triboelectric nanogenerator

Received: April 16, 2024
Revised: June 6, 2024
Published online: June 23, 2024

[1] X. Fang, S. Misra, G. Xue, D. Yang, *IEEE Commun. Surv. Tutorials* **2012**, *14*, 944.
[2] L. Xie, T. Huang, P. R. Kumar, A. A. Thatte, S. K. Mitter, *Proc. IEEE* **2022**, *110*, 1940.
[3] K. Li, X. Yan, Y. Han, *Appl. Soft Comput.* **2024**, *150*, 111033.
[4] Q. Wang, Z. Zhang, Q. Chen, J. Zhang, S. Kang, *Sensors* **2024**, *24*, 565.
[5] A. Rezaee Jordehi, S. A. Mansouri, M. Tostado-Véliz, A. Ahmarinejad, F. Jurado, *Int. J. Hydrogen Energy* **2024**, *50*, 175.
[6] L. Xie, X. Zheng, Y. Sun, T. Huang, T. Bruton, *Proc. IEEE* **2023**, *111*, 762.
[7] H. Liu, Y. Chen, N. Cui, D. Xu, J. Li, *IEEE Internet Things J.* **2022**, *9*, 22256.
[8] P. Glaum, F. Hofmann, *Appl. Energy* **2023**, *343*, 121199.
[9] J. Zhou, Y. S. Geng, X. G. Wang, *AMM* **2013**, *321–324*, 1396.
[10] M. S. Kwak, M. Peddigari, Y. Min, J.-J. Choi, J.-H. Kim, M. A. Listyawan, J. Ryu, G.-T. Hwang, W.-H. Yoon, J. Jang, *Nano Energy* **2022**, *101*, 107567.
[11] O. Cetinkaya, O. B. Akan, *IEEE Wireless Commun.* **2017**, *24*, 34.
[12] Y. Liu, Y. Yu, N. Gao, F. Wu, *Engineering* **2020**, *6*, 778.
[13] M. Mussi, *J. Energy Storage* **2024**, *82*, 110572.
[14] Y. Sun, G. Szűcs, A. R. Brandt, *Energy Environ. Sci.* **2018**, *11*, 1811.
[15] Q. Wang, J. Zhou, K. Wang, Q. Lin, D. Xu, G. Wen, *Int. J. Mech. Sci.* **2023**, *250*, 108284.
[16] M. Liu, Y. Zhang, H. Fu, Y. Qin, A. Ding, E. M. Yeatman, *Appl. Energy* **2023**, *337*, 120908.
[17] K. Moradian, T. F. Sheikholeslami, M. Raghebi, *Energy Convers. Manage.* **2022**, *266*, 115824.
[18] S. K. Karan, R. Bera, S. Paria, A. K. Das, S. Maiti, A. Maitra, B. B. Khatua, *Adv. Energy Mater.* **2016**, *6*, 1601016.
[19] D. Hu, M. Yao, Y. Fan, C. Ma, M. Fan, M. Liu, *Nano Energy* **2019**, *55*, 288.
[20] M. A. Johar, A. Waseem, M. A. Hassan, I. V. Bagal, A. Abdullah, J. Ha, S. Ryu, *Adv. Energy Mater.* **2020**, *10*, 2002608.
[21] Y. Zhang, H. Wang, L. Wang, *Rev. Sci. Instrum.* **2023**, *94*, 085001.
[22] J. Chen, G. Zhu, W. Yang, Q. Jing, P. Bai, Y. Yang, T. Hou, Z. L. Wang, *Adv. Mater.* **2013**, *25*, 6094.
[23] H. Yang, M. Deng, Q. Zeng, X. Zhang, J. Hu, Q. Tang, H. Yang, C. Hu, Y. Xi, Z. L. Wang, *ACS Nano* **2020**, *14*, 3328.
[24] H. Yu, Z. Xi, Y. Zhang, R. Xu, C. Zhao, Y. Wang, X. Guo, Y. Huang, J. Mi, Y. Lin, T. Du, M. Xu, *Nano Energy* **2023**, *107*, 108182.
[25] W. Yang, Q. Gao, X. Xia, X. Zhang, X. Lu, S. Yang, T. Cheng, Z. L. Wang, *Extreme Mech. Lett.* **2020**, *37*, 100718.
[26] M. S. Kwak, M. Peddigari, H. Y. Lee, Y. Min, K. Park, J. Kim, W. Yoon, J. Ryu, S. N. Yi, J. Jang, G. Hwang, *Adv. Funct. Mater.* **2022**, *32*, 2112028.
[27] S. M. S. Rana, M. Salauddin, M. Sharifuzzaman, S. H. Lee, Y. D. Shin, H. Song, S. H. Jeong, T. Bhatta, K. Shrestha, J. Y. Park, *Adv. Energy Mater.* **2022**, *12*, 2202238.
[28] C. Hu, Y. Yang, Z. L. Wang, *Nano Energy* **2022**, *103*, 107760.
[29] X. Wang, X. Liang, Z. Hao, H. Du, N. Zhang, M. Qian, *Mech. Syst. Signal Process.* **2016**, *72–73*, 906.
[30] Z. Xu, L. N. Y. Cao, C. Li, Y. Luo, E. Su, W. Wang, W. Tang, Z. Yao, Z. L. Wang, *Nat. Commun.* **2023**, *14*, 2792.
[31] A. Yu, P. Jiang, Z. Lin Wang, *Nano Energy* **2012**, *1*, 418.
[32] C. Wang, X. Zhang, J. Wu, X. Yu, T. Cheng, H. Ma, Z. L. Wang, *Mech. Syst. Signal Process.* **2022**, *166*, 108429.
[33] L. Fang, Q. Zheng, W. Hou, L. Zheng, H. Li, *Nano Energy* **2022**, *97*, 107164.

[34] Y. Qi, J. Zhao, J. Zeng, X. Cao, Y. Qin, J. Cao, L. Gong, X. Huang, Z. Wang, G. Liu, C. Zhang, *ACS Appl. Mater. Interfaces* **2023**, *15*, 40569.
[35] W. Zhang, X. Zhang, Y. Yu, X. Cheng, H. Li, S. Liu, L. Meng, Z. L. Wang, T. Cheng, *Adv. Energy Mater.* **2023**, *13*, 2302838.
[36] S. Gao, S. Feng, J. Wang, H. Wu, Y. Chen, J. Zhang, Y. Li, R. Wang, X. Luo, H. Wei, X. Zeng, *ACS Appl. Mater. Interfaces* **2023**, *15*, 34764.
[37] Z. Yuan, X. Jin, R. Li, B. Wang, C. Han, Y. Shi, Z. Wu, Z. L. Wang, *Small* **2022**, *18*, 2107221.
[38] S. Gao, X. Zeng, G. Zhang, J. Zhang, Y. Chen, S. Feng, W. Lan, J. Zhou, Z. L. Wang, *Nano Energy* **2022**, *101*, 107530.
[39] H. Wu, J. Wang, Z. Wu, S. Kang, X. Wei, H. Wang, H. Luo, L. Yang, R. Liao, Z. L. Wang, *Adv. Energy Mater.* **2022**, *12*, 2103654.
[40] X. Zhang, Y. Yu, X. Xia, W. Zhang, X. Cheng, H. Li, Z. L. Wang, T. Cheng, *Adv. Energy Mater.* **2023**, *13*, 2302353.